Nano/microcharacterization and image analysis on bonding behaviour of ITZs in recycled concrete enhanced with waste glass powder

Hanbing Zhao [a], Wengui Li [a,*], Yixiang Gan [b], Kejin Wang [c], Zhiyu Luo [d]

[a] School of Civil and Environmental Engineering, University of Technology Sydney, NSW 2007, Australia
[b] School of Civil Engineering, The University of Sydney, Camperdown, NSW 2006, Australia
[c] Department of Civil, Construction and Environmental Engineering, Iowa State University, IA 50011, USA
[d] Department of Civil and Environmental Engineering, National University of Singapore, 117567, Singapore

ABSTRACT

Waste glass powder (WGP) has been shown to help improve concrete properties. However, the underlying mechanism needs to be explored at the micro level, specifically on the interfacial transition zones (ITZs). This study aims to investigate the microtopography and bonding behaviours of ITZs using modelled recycled aggregate concrete (MRAC). To highlight the differences, two sets of MEAC were prepared, consisting of old and new mortars with water-cement ratios of 0.45 and 0.40, respectively. WGP was incorporaed in the new mortar, replacing 20 wt% of cement to enhance the performance of the new ITZ. Two groups of MRAC with three types of ITZs were successfully fabricated and studied. The property differences between the old ITZ, new ITZ without WGP, and new ITZ with WGP were comprehensively evaluated and compared based on phase distribution, chemical composition, and micromechanical properties. The results show that the new ITZ without WGP exhibited the highest porosity (avg. 7.29%) but a higher calcium silicate hydrate (C-S-H) elastic modulus (avg. 11.89 GPa) compared to the old ITZ (avg. 4.33% and 10.37 GPa, respectively). WGP effectively reduced the volume fraction of pores and cracks to 4.30% by reacting with calcium hydroxide (CH) within the new ITZ and the adjacent old mortar, resulting in generation of a significant amount of C-S-H gel with a Si/Ca ratio of approximately 1.5. To obtian more accurate results regarding the bonding strength between the old and new mortars, it is necessary to further evaluate the cohesion of C-S-H and the compactness of the new ITZ in a comprehensive manner.

1. Introduction

1.1. Recycled aggregate and waste glass

In recent years, researchers devoted themselves to finding novel and environmentally friendly construction materials [1]. As a resource-intensive material, concrete consumes a large amount of natural sand, gravel and cement every year [2]. Natural aggregates are not renewable, and conventional Portland cement production aggravates CO_2 emissions [3]. Meanwhile, hard degradable construction and municipal (C&M) waste such as crushed waste concrete and waste glass are occupying space in landfills [1,4]. Recycling these waste materials and applying them in concrete production is undoubtedly an effective way to maximize environmental benefits.

Researchers have attempted to recycle crushed waste concrete and waste glass powder (WGP) as substitutes for natural coarse aggregate (NCA) and cement, respectively [5–7]. Existing research results indicate that the old mortar on the surface of recycled coarse aggregate (RCA) is responsible for the weak bond strength with the new mortar matrix, resulting in lower mechanical and durable properties of recycled aggregate concrete (RAC) [8,9]. On the other hand, a large amount of amorphous silica in WGP is an important substance for pozzolanic reaction, similar to the role of supplementary cementitious materials (SCM, such as fly ash, slag and nano-SiO_2) commonly used in the cement industry [3,10–12]. Omran et al. [13] and Islam et al. [14] reported that 20% of cement replaced by WGP can improve the compressive strength of concrete.

To deeply explain the behaviour mechanism of sustainable concrete under mechanical loading and aggressive environments, it is necessary to explore concrete physical and chemical properties from a microscopic

level, especially the properties of interfacial transition zones (ITZs) [15]. The concrete internal structure can be roughly divided into three phases: the coarse aggregate, the mortar matrix and the ITZ between the two regions [16]. The composition types of ITZ are the same as the mortar matrix, but the characteristics are slightly different [17]. Due to the 'wall effect' and bleeding of aggregate, water-cement ratio, porosity and alkaline crystalline phases of ITZ are higher than mortar matrix [18]. Therefore, ITZ is usually regarded as the weakest area in concrete, which is the key to studying concrete mechanical and ion transport performance.

RAC possesses more ITZs than NAC, among which, researchers mostly focus on the old ITZ adjacent to NCA and the new ITZ between the old mortar on the RCA and the new mortar [19,20]. Numerous existing instrumentation techniques such as Scanning electron microscope (SEM-based) characterisation and nanoindentation provide a realistic basis for the determination of ITZ width and understanding its characteristics from multiple dimensions [21]. Xiao and Li et al. [22,23] investigated the micromechanical properties of old and new ITZs in RAC by nanoindentation technique. After extensive testing, it was determined that the thickness of the new and old ITZs in RAC were around 40–50 μm and 55–65 μm respectively [22,23]. In addition, the elastic modulus of old ITZ was about 70–80% of old mortar, and the elastic modulus of new ITZ was about 80–90% of new mortar [22,23]. Bosque et al. [24] compared the results of electron microscopy and nanoindentation tests and found that the thickness of new ITZ measured by nanoindentation was 50–60 μm, which was smaller than the value obtained by Scanning electron microscope-Energy dispersive spectrometer (SEM-EDS).

When a small amount of WGP is added to concrete, the active silica in glass participates in the pozzolanic reaction to generate C-S-H, which contributes to improving the strength of ITZ [25,26]. Kong et al. [27] found that there was more C-S-H in the ITZ of concrete containing 30% WGP. Du and Tan [28] also pointed out that fine soda-lime glass powder can react with CH in concrete to form C-S-H gel. Concrete with 15–30% of cement replaced by WGP had a more compact and homogeneous ITZ microstructure [28]. For higher WGP content and insufficient CH, the excess WGP can block channels to reduce the water and ions penetration depth [28].

1.2. Innovation of modelled aggregate concrete

Most existing studies on the microscopic properties of RAC with WGP are based on irregular aggregate [29]. However, rough and angular aggregate surface brings severe challenges to the research of ITZ [30]. In nanoindentation tests, for example, the indenter may touch the aggregate hidden under the surface cement paste [31]. The number of test points available for ITZ analysis in each column of grid nanoindentation is different [30]. It is also difficult to determine the distance of each row of test points from the aggregate boundary [30]. Testers have to reduce indentation depth and increase the density of the grid. This greatly increases the workload and makes it difficult to achieve accurate statistical results [21]. SEM-based analysis faces a similar problem. It is well-known that the formation of ITZ is attributed to the 'wall effect' of aggregate [32]. The uneven surface of aggregate is destined to the heterogeneity and complexity of ITZ [30,31]. In addition, the bleeding around the aggregate seriously affects the properties of ITZ at different locations [5]. This requires researchers to extract a large number of ITZ images at different positions to obtain a passable average result.

To solve the above problems, Shah and Winter [33] are the first to propose a novel modelled concrete with cylindrical aggregate for analysing the inelastic mechanical properties of concrete. Subsequently, Xiao et al. [34] extended the study of this concrete to the microscopic level. In recent years, Luo et al. [30,31], Fu et al. [35], and Zhan et al. [36] used a similar concept to simulate ITZ by aggregate blocks and obtained satisfactory microstructure, chemical composition and micromechanical performance test results. It has to be admitted that the ITZ

simulated by modelled concrete idealises the actual situation and ignores the randomness and complexity of the real ITZ [30,31]. However, with the help of characteristics of modelled concrete, the bonding mechanism of aggregate and mortar can be more effectively explored.

2. Research scope and significance

The old mortar attached to the surface of the recycled aggregate makes the surface rougher, which increases the uncertainty of the new ITZ study between old mortar and new mortar. In this case, transferring the research object from the real ITZs to the simplified ITZs in the model sample can greatly improve the research efficiency. However, few researchers fabricated MRAC samples successfully for ITZ performance studies. Although Zhan et al. [36] produced similar samples, they used cement paste as recycled aggregate, calling it modelled recycled concrete aggregate instead of MRAC (containing old and new ITZs). In addition, the bonding properties between old mortar and new mortar with WGP are still unknown. Therefore, referring to the previous experimental experience [30,31,36,37], three regular ITZs (old ITZ, new ITZ with and without WGP) were manufactured through MRAC in this study. The ITZ width was identified by Backscattered electron (BSE) combined with image analysis. Subsequently, the differences in chemical composition and micromechanical properties were systematically tested by Energy dispersive spectrometer (EDS), Thermogravimetry analysis (TGA), Nuclear magnetic resonance spectrometer (NMR) and nanoindentation techniques to evaluate the improving performance of WGP within the new ITZs.

This study contributed to more accurately and efficiently exploring the cohesion of multiple ITZs in RAC by observing the micromorphology and constituent distribution. In addition, the enhancing mechanism of WGP on the new ITZ of RAC was comprehensively evaluated from multiple dimensions. This study is beneficial to enhance the understanding of the efficacy of WGP in RAC and promote the recycling application of WGP in structural construction materials [68–70].

3. Experimental program

3.1. Materials and mixture proportion

A MRAC sample consists of three parts: a rectangular granite block, old mortar on the surface of the stone block, and new mortar on the outermost layer of the sample. The schematic diagram of MRAC is shown in Fig. 1. Rectangular granite blocks were seen as virgin coarse aggregate. Fine aggregate in the old and new mortar was silica sand with a fineness modulus of 1.9. General purpose Portland cement was used as the main cementitious material. In the MRAC sample with WGP, 20% of cement in the new mortar was replaced by milled waste soda-lime glass powder with average particle size of 50 μm. The particle size distribution and oxide composition of cement and WGP are shown in Fig. 2. and
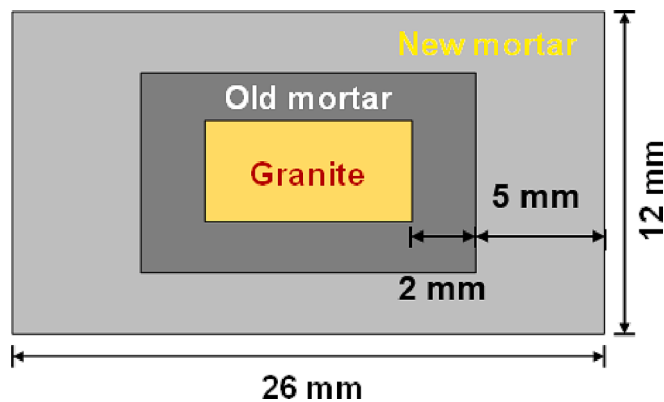
Fig. 1. Schematic diagram of MRAC.
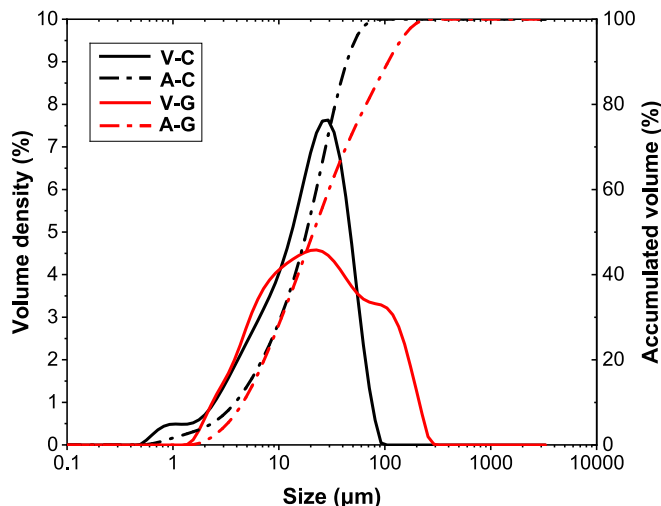
Fig. 2. Particle size distribution of cementitious materials tested by Mastersizer 3000.

Table 1, respectively. Considering that the interface between old and new mortar may be difficult to distinguish under an electron microscope, different water-cement ratios were designed in the preparation of new and old mortar. According to previous studies, the strength of RAC is normally lower than that of NAC under the same conditions [38]. Civil engineers usually reduce water-cement ratio of new mortar or choose cement with higher strength grade to ensure that the RAC structures meet the strength requirements [1]. Therefore, the water-cement ratios of old and new mortars in this study were designed to be 0.45 and 0.4, respectively. The detailed mix proportion of new and old mortar is shown in Table 2.

3.2. Sample preparation

According to previous experience [30,31,37], the main steps of MRAC sample preparation were designed and shown in Fig. 3. Granite gravels with appropriate size were selected and ground on 320 grits abrasive papers into 13 mm × 13 mm × 8 mm rectangular blocks. Then, the surface of the granite blocks was smoothed by 600, 800 and 1200 grits abrasive papers with each grade lasting for 15 min. 0.3 μm and 0.05 μm alumina slurry were used to polish granite blocks under a small force, and the polish process lasted for 1 h. After grinding and polishing, granite blocks were cleaned in an ultrasonic bath for 3 min to remove alumina particles on the surface of samples. The processed granite blocks are called modelled NCA. According to the mix proportion in Table 2, the saturated surface dried modelled NCA were covered with old mortar in Φ25 mm cylindrical moulds and discharged air bubbles in the mortar by tapping. After curing in the mould for one day, samples were put in a moist environment at 23 ± 3 ℃ for 28 days. Grinding and polishing were consistent with the above-mentioned processes of modelled NCA. Then, new mortar with/without WGP was prepared and covered around the modelled RCA. After 28 days, the MRAC with old and new mortar was ground and put in Φ35 mm cylindrical moulds and poured with epoxy resin. After one day, samples were wet-cut by a low-speed diamond saw under the protection of hardened epoxy resin to expose old and new ITZs into the air. Finally, samples were coated with an additional layer of epoxy resin. The surface waiting for observation

was ground and polished. It should be noted that to avoid the height difference between the aggregate and mortar caused by excessive polishing, the entire polishing time was reduced to 30 min [39]. Photos of MRAC manufacturing process are presented in Fig. 4. The modelled samples were used for Backscattered Electron-Energy dispersive spectrometer (BSE-EDS) tests and nanoindentation. After that, the new mortar was cut out and ground into powder for Thermogravimetric-derivative thermogravimetry (TG-DTG) and Nuclear magnetic resonance spectrometer (^{29}Si NMR) tests.

3.3. Experimental methods

3.3.1. BSE-EDS tests

A scanning electron microscope (SEM, Zeiss EVO LS15) equipped with a BSE image detector was used to randomly extract images of ITZs. The accelerating voltage and working distance were set as 15 kV and 10 mm respectively. For each ITZ, 30 BSE images at 500 × magnification were used to statistically analyse the volume fraction of constituents [30,39]. The brightness and contrast of BSE images of each ITZ were kept consistent to reduce the workload of image analysis. EDS data were acquired at accelerating voltage consistent with BSE and lower probe current. EDS mapping was used to show phase distribution. In addition, stoichiometric quantification with P/B-ZAF on Si, Ca and Na was conducted to deeply analyse the element ratio within ITZs and adjacent mortar matrix.

3.3.2. TG-DTG tests

TG tests were conducted by NETZSCH STA 449 F3 Jupiter. 20–30 mg sample powder was weighed in an alumina crucible, and then kept in a 40 ℃/N_2 environment. After maintaining this environment for 30 min, the temperature in the furnace was heated to 1000 ℃ at a speed of 10 ℃/min, and the mass loss of the sample powder between 50 and 1000 ℃ was obtained. The TG curves were derived to highlight the relative content differences of C-S-H, Portlandite and Calcite in different groups of samples.

3.3.3. ^{29}Si NMR tests

Agilent 500 MHz Nuclear Magnetic Resonance (NMR) was used to acquire solid-state ^{29}Si spectra from −50 to −150 ppm. The measurements were conducted in a 4 mm rotor at 71.4 kHz spinning rate and 30 s relaxation delays. The statistical deconvolution of ^{29}Si NMR spectra based on the Gaussian model was applied to obtain Q^0-Q^2 for unhydrated cement clinkers and C-S-H gel content analysis.

3.3.4. Nanoindentation

Nanoindentation tests on ITZs were carried out by an Agilent G200

Table 2
Mix proportions of MRAC.

Mix ID	Phases	Cement (g)	Glass (g)	Sand (g)	Water (g)	Granite
MRAC-C	Old mortar	100	0	150	45	1
	New mortar	100	0	150	40	
MRAC-G	Old mortar	100	0	150	45	1
	New mortar	80	20	150	40	

Table 1
Oxide composition of cement and WGP measured by X-ray fluorescence.

Composition (%)	CaO	SiO₂	Al₂O₃	SO₃	Fe₂O₃	MgO	K₂O	Na₂O	LOI
Cement	64.9	18.6	4.1	3.0	3.1	1.6	0.5	–	4.2
WGP	10.8	68.4	0.9	0.1	0.4	1.8	0.3	13.5	3.8
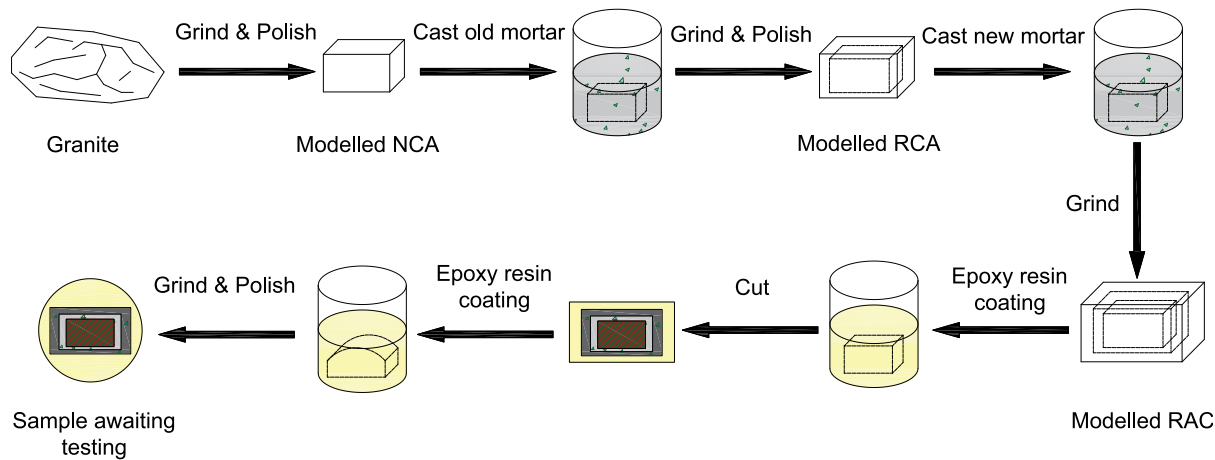
Fig. 3. Process of MRAC sample preparation.

(a) Casting mortar

(b) Modelled RAC after surface polishing

(c) Cutting modelled sample with epoxy resin

(d) modelled sample after grinding and polishing
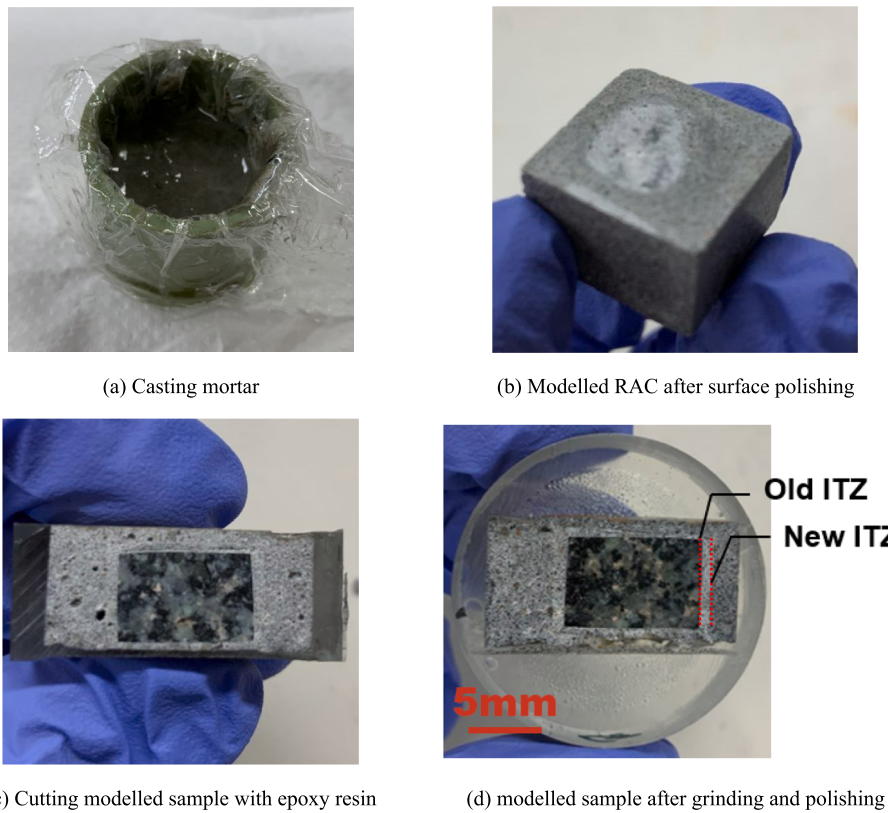
Fig. 4. Preparation of modelled recycled aggregate concrete.

Nano Indenter. Due to the heterogeneous structure of cement-based materials, it may be difficult to obtain accurate micromechanical properties of ITZ under shallow indentation tests [30]. If the indentation depth is too deep, the indentation area of a single point would be too large to ensure that enough indentation points are conducted within ITZs. Comprehensively comparing the previous research data and according to the requirements in ASTM E384-17 (Standard test method for microindentation hardness of materials), the indentation depth of each testing point was set to 800 nm [30]. The vertical spacing of testing points was 15 μm. The horizontal spacing of the testing points near the boundary between aggregate and ITZ was 8 μm, and the horizontal spacing between the remaining testing points was 7 μm. No testing points were designed at the boundary to avoid the interference of sudden change of hardness on the results.

The layout of the testing points and a typical depth-load curve on old ITZ are shown in Fig. 5. The nanoindentation depth-load curve was not deformed, indicating that the flatness of the sample after polishing meets the test requirements of nanoindentation. Five of these 14×5 grid nanoindentation tests were performed for each ITZ [30]. The nano-indentation force loading procedure was based on the depth control method. When the indentation depth was close to 800 nm, the load was sustained at the peak value for 10 s, and then gradually unloaded to 10% of the peak load after reaching the target depth. The elastic modulus and hardness of ITZs can be calculated by indentation load (P), indentation depth (h), reduced elastic modulus (E_r), projected area (A) and characteristics of the diamond indenter tip (elastic modulus, E_i and Poisson's ratio, V_i) according to Eqs. (1) to (3) adopted by previous researchers [22,40]. The Poisson's ratio of cement paste (v) was set as 0.2. This study
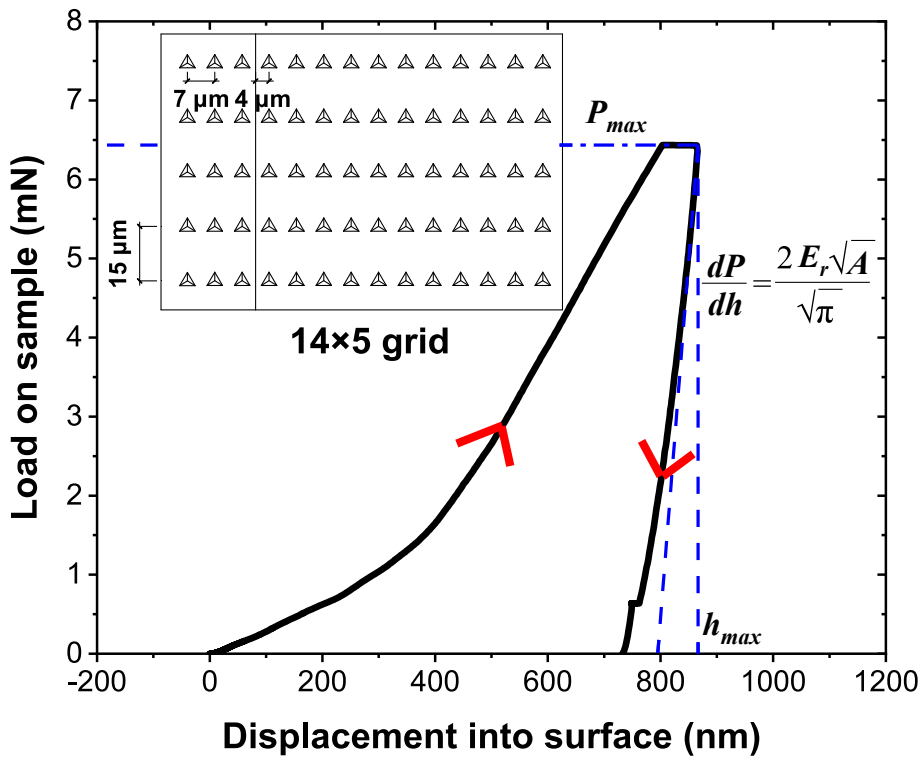
Fig. 5. Grid nanoindentation and a typical load-depth curve.

focused on the cohesion strength of ITZ, so the test avoided regions close to fine aggregate and large cracks. The test results of each column were averaged as the results.

$$H = \frac{P_{max}}{A} \tag{1}$$

$$S = \left.\frac{dP}{dh}\right|_{h=h_{max}} = \frac{2}{\sqrt{\pi}} E_r \sqrt{A} \tag{2}$$

$$\frac{1}{E_r} = \frac{1-v^2}{E} + \frac{1-v_i^2}{E_i} \tag{3}$$

4. Results and analysis

4.1. Phases distribution of ITZs

Fig. 6 shows typical BSE images of three ITZs in this study. Compared with common SEM images, BSE is easier to distinguish between phases in cement-based materials according to grey value, even though the resolution of BSE image may be lower than SEM images [41]. Many researchers have adopted BSE images combined with image analysis techniques to investigate the constituent distribution in ITZs [41–43].

Taking the old ITZ as an example, Fig. 7 shows the schematic view of BSE image processing for statistical analysis. The boundary between the aggregate and the matrix can be easily captured manually and the aggregate part can be removed by Photoshop. For the remaining mortar matrix region, the image analysis software, Image Pro was used to acquire its grey value-area segmentation curve. Wong's grey value segmentation method was adopted [44–46]. The grey value threshold and different phases can be identified by the intersection between the two liner fittings at the inflection of the cumulative area curve with grey values, as shown in Fig. 7 (b). The image after phase segmentation is shown in Fig. 7 (c) (red represents pores and cracks; green represents reaction products; blue represents unreacted products). The matrix within 100 μm from the aggregate boundary was continuously divided

(a) Old ITZ

(b) New ITZ without WGP

(C) New ITZ with WGP
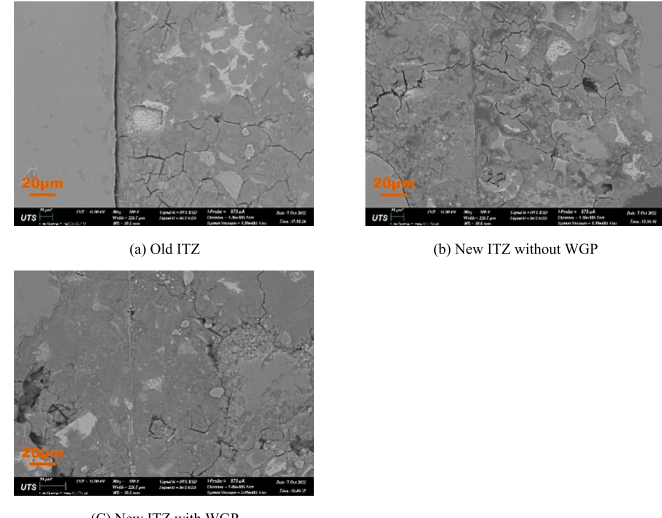
Fig. 6. BSE images of old and new modelled ITZs.

into 20 strips with a width of 5 μm. For each ITZ, 30 BSE images were selected for statistical analysis of phase volume fraction within ITZ and a part of the mortar matrix.

The volume fractions of unreacted products, reaction products and pores/cracks are shown in Fig. 8 as stacked area graphs. The 'wall effect' can be clearly detected by observing the volume fraction change of unreacted products from the aggregate surface to mortar matrix. The content of unreacted products in the region close to the aggregate surface was lower and the percentage gradually improved to a stable value with the increase of distance to the aggregate surface. Compared to pores and cracks, reaction and unreacted product contents have a lower variability degree at different positions [18]. As a result, the ITZ width can be determined according to the volume fraction of unreacted

(a) Aggregate region removal

(b) Grey threshold determination

(c) Phases segmentation

(d) Strips division
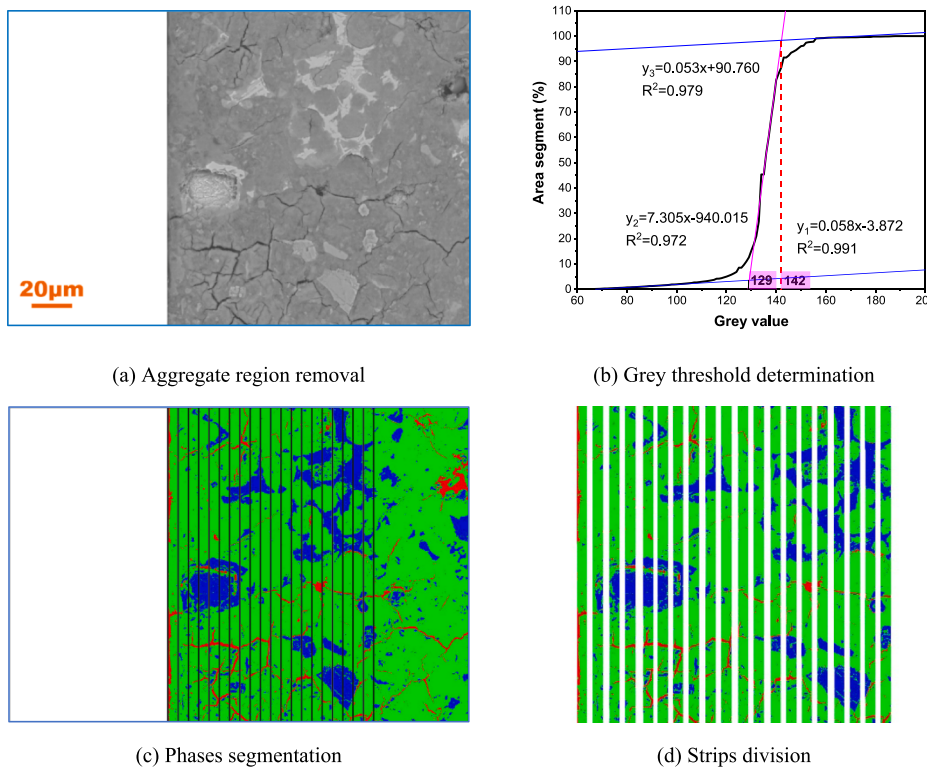
Fig. 7. Schematic view of BSE image processing.

products [18,30]. Taking the middle of the strips as the coordinate points, the region where the content of unreacted products increased significantly was identified as ITZ. Therefore, the widths of old ITZ, new ITZ with and without WGP were 52.5, 37.5 and 22.5 μm, respectively. The width of the new ITZ without WGP was narrower than the old ITZ, probably because the lower water-cement ratio designed in the new mortar improved the properties of the matrix [22]. Comparing the volume fractions of reaction and unreacted products in ITZs, it is seen that the content of unreacted products in the new ITZ without WGP was 11.98%, lower than 14.60% of the old ITZ. However, the volume fractions of reaction products were similar, both around 80.5%, because of the higher proportion of pores and cracks (7.29%) within the new ITZ without WGP than about 4.33% of the old ITZ. The surface of old mortar was looser and more porous than natural granite aggregate, and it was difficult to form a dense bonding between old and new mortar [47]. In comparison, the width, unreacted products, and void volume fractions in new ITZ containing WGP were significantly reduced to 22.5 μm, 10.27% and 4.30% respectively. Correspondingly, the proportion of reaction products increased to 85.43%, indicating that WGP can effectively reduce the volume of ITZ in RAC and improve the bonding performance between new mortar and RCA surface. By observing the volume fraction of pores and cracks in three ITZs, the volume fraction close to the aggregate surface was obviously higher than in other regions and decreased rapidly within 10 μm from the aggregate surface. This is not only due to the 'wall effect' improving local water-cement ratio, the self-shrinkage of cement paste was more obvious than aggregate because of lower elastic modulus [30]. Some researchers have even discovered the debonding phenomenon between mortar and aggregate [48,49]. This proves the feasibility of the image analysis technique in this work from another aspect.

To conduct a more detailed statistical analysis of the phases within the ITZ, the analysis of variance (ANOVA) proposed by R.A. Fisher was used to evaluate the difference significance between ITZ-mortar matrix and ITZ-ITZ. The F value in ANOVA represents the ratio of the between-group mean variance to the within-group mean variance [50]. The larger F value means a significant difference between the two groups of data [50]. However, the P value can more intuitively reveal the difference between two groups of data. Each F value corresponds to a P value. A P value higher than 0.05 indicates that the two groups of data are similar [51]. Otherwise, it is believed that there is a significant difference between the two groups of data, and when the P value is less than 0.01, it can be considered that the difference between the two groups of data is extremely significant [51]. The statistical results of the volume fraction of phases between ITZ-mortar matrix and ITZ-ITZ are shown in Table 3.

The data shows that the content of reaction/unreacted products between old ITZ and old mortar matrix was significantly different. This was equally evident between the new mortar matrix and the new ITZ without WGP. The volume fractions of reaction and unreacted products directly reflect the performance of ITZs [18]. It can be inferred from the statistical results that the characteristics of pure cement-based ITZ were obviously weaker than the mortar matrix. In comparison, the content of reaction/unreacted products in the new mortar matrix and new ITZ with 20% WGP were similar, while the proportions of pores and cracks were obviously different, indicating that WGP can effectively refine the percentage of reaction and unreacted products, but the ability to reduce porosity in ITZ was insufficient. Nevertheless, it still can be seen from Fig. 8 that the volume fraction of pores and cracks in the ITZ with WGP was lower than that of old mortar and new mortar without WGP.

Table 4 presents the statistical results of phase differences among ITZs. The difference of phases between old ITZ and new ITZ without WGP was not obvious. However, the volume fraction of reaction products was significantly different in the new ITZs with and without WGP. Combining with Fig. 8, it can be seen that the increase in the volume fraction of reaction products in the new ITZ with WGP was the result of the decrease in both the proportion of pores/cracks and unreacted products. Therefore, the difference in the content of the reaction products within the two groups of new ITZ was the most obvious.

(a) Old ITZ

(b) New ITZ without WGP

(c) New ITZ with WGP
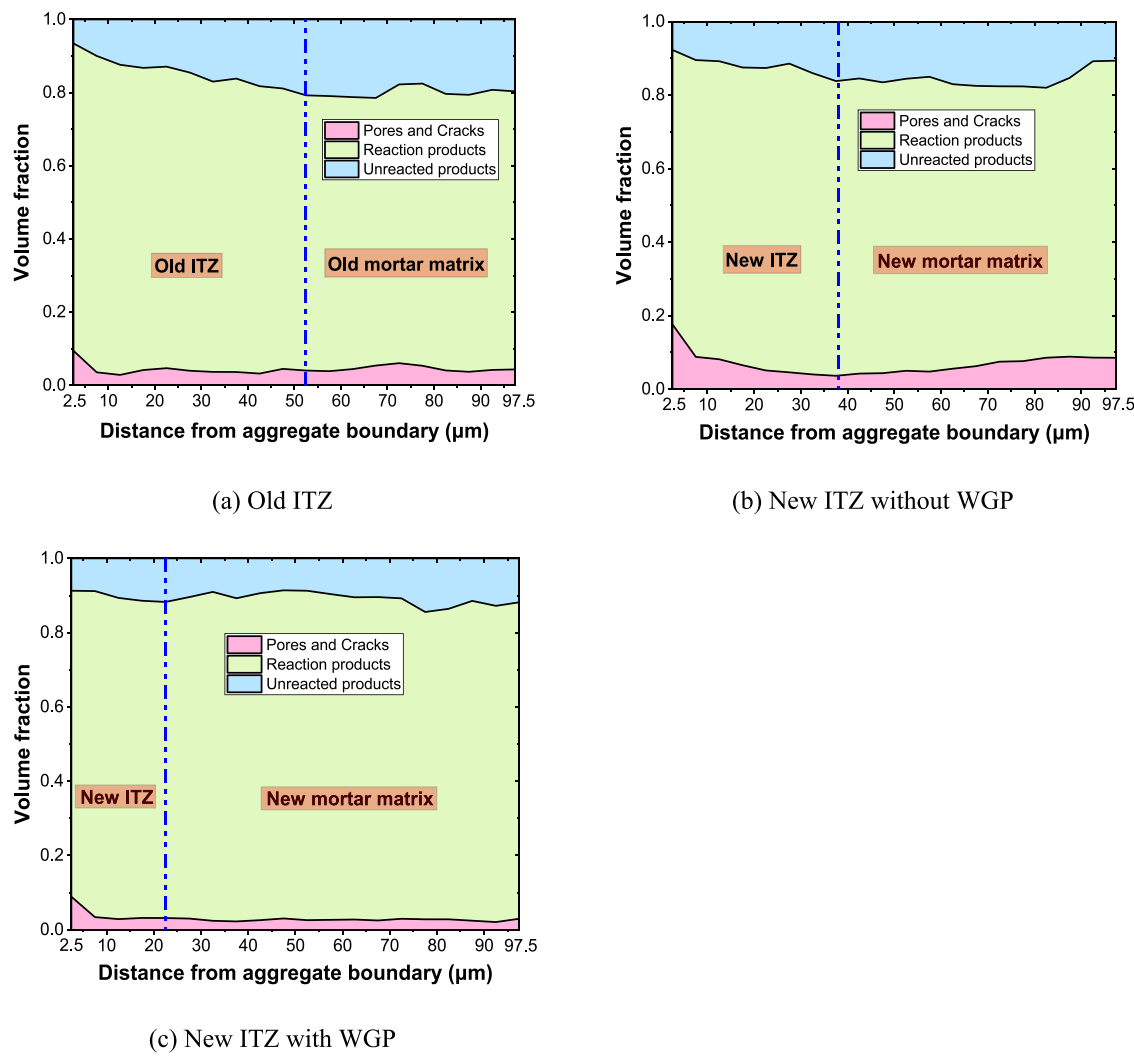
Fig. 8. Phases volume fraction from aggregate boundary to the mortar matrix.

Table 3
Difference comparison of phases between ITZ and mortar matrix.

	Pores and cracks		Reaction products		Unreacted products	
	P value	F value	P value	F value	P value	F value
Old ITZ Old mortar matrix	0.68204	0.17339	2.44×10^{-4}**	20.76867	0.00202**	13.00413
New ITZ without WGP New mortar matrix without WGP	0.66176	0.19785	0.02505*	5.97313	0.00543**	9.98152
New ITZ with WGP New mortar matrix with WGP	0.01994*	6.52166	0.2609	1.3474	0.53176	0.40653

Note: The symbol '*' and '**' represent significant difference and extremely significant difference between two groups of data, respectively.

Table 4
Difference comparison of phases between ITZs.

	Pores and cracks		Reaction products		Unreacted products	
	P value	F value	P value	F value	P value	F value
Old ITZ New ITZ without WGP	0.065	3.8921	0.81863	0.05424	0.13371	2.48027
New ITZ without WGP New ITZ with WGP	0.2115	1.76007	0.00662**	11.13918	0.19851	1.87228

Note: The symbol '*' and '**' represent significant difference and extremely significant difference between two groups of data, respectively.

4.2. Chemical and mineralogical composition of ITZs

4.2.1. EDS element mapping analysis

Considering that soda-lime WGP was used as an additive in this study, in addition to the main elements (Al, Si, Ca) belonging to cement-based materials, the distribution of Na is also presented in Fig. 9 by EDS mapping. The natural aggregate used in this research was granite, whose main component was silica and feldspar. The boundary between natural aggregate and old mortar can be easily distinguished by the observation of Al, Si, Na distribution in Fig. 9 (a). Granite possesses an extremely low water absorption ratio. Free water attached below the surface of granite is easy to bleed into ITZs and form a local high water-cement ratio region with less Al, Si and Ca content near the boundary of aggregate, as shown in Fig. 9 (a). This is an important reason why the cohesion of C-S-H in ITZ is weaker than that in the mortar matrix [52]. Al was mainly distributed in some phases, such as C-A-S-H, which is consistent with the distribution of Al in previous cement paste samples [21,38]. In addition, Si and Ca were dispersed in ITZs uniformly in old ITZ and new ITZ without WGP, indicating that cement in these two regions had high degree of hydration. In comparison, there were obvious Si and Na rich zones in the new ITZ with WGP, which were incompletely reacted glass clinkers, and the proportion increased with the distance to the boundary of old mortar. This is consistent with the unreacted products distribution in Fig. 8 (c) and previous studies on the fly ash clinkers distribution in

ITZs of geopolymer concrete [18,31]. According to Chen et al. [53] and Du et al. [28], the pozzolanic reaction involved in WGP is a long process, which may last for one year or more. However, this did not prevent the amorphous silica in small-size and parts of large-size glass clinkers from dissolving and reacting with CH to form more C-S-H gel, which improved the performance of ITZ [29].

4.2.2. EDS element quantitative analysis

Numerous areas were randomly selected, and more than 10,000 points were extracted for quantitative analysis of EDS results. The Si/Ca vs. Si/Na atomic ratios of effective points in ITZs and the adjacent matrix were collected and shown in Fig. 10. Except several data points close to 0 may represent pores or cracks, the densest point cluster within the blue ellipse represents C-S-H gel. The centre of the ellipse was marked with a red dot. It can be clearly seen from Fig. 10 (a) that the number of effective points in the old ITZ was lower than that in other regions, indicating that the constituents in the old ITZ was relatively loose. The number of effective points in the corresponding old mortar matrix increased significantly, and the average Si/Ca ratio of C-S-H was about 1.2, higher than that of the old ITZ (0.6 on average). It has been known that C-S-H exhibits a better performance with a higher Si/Ca ratio, which is consistent with the common knowledge that ITZ is the weakest region in concrete [54]. Since a lower water-cement ratio was designed to prepare new mortar, the distance between cement clinkers in the new
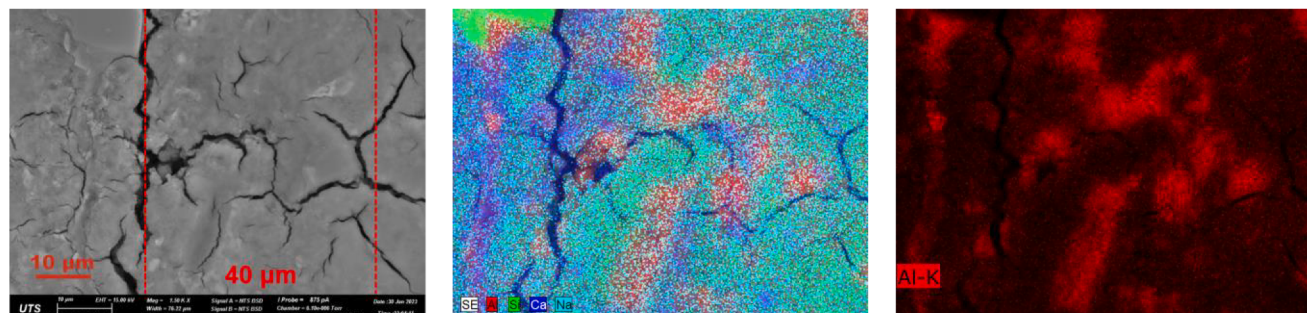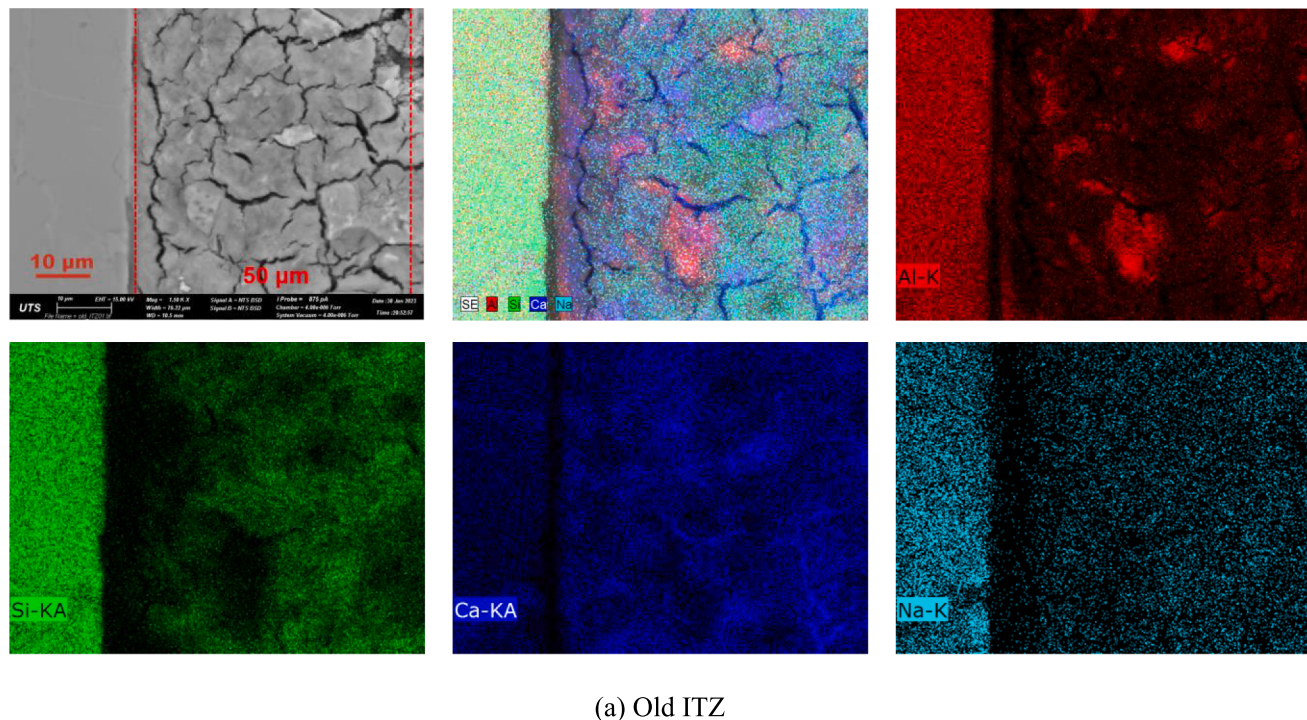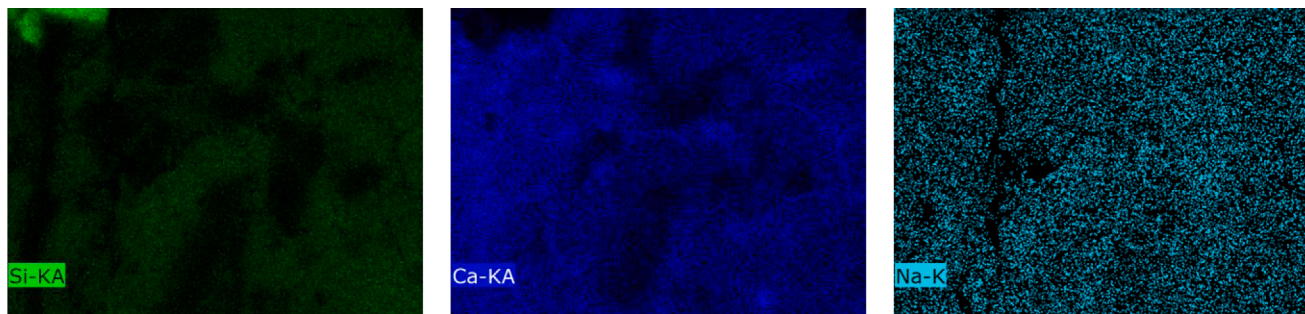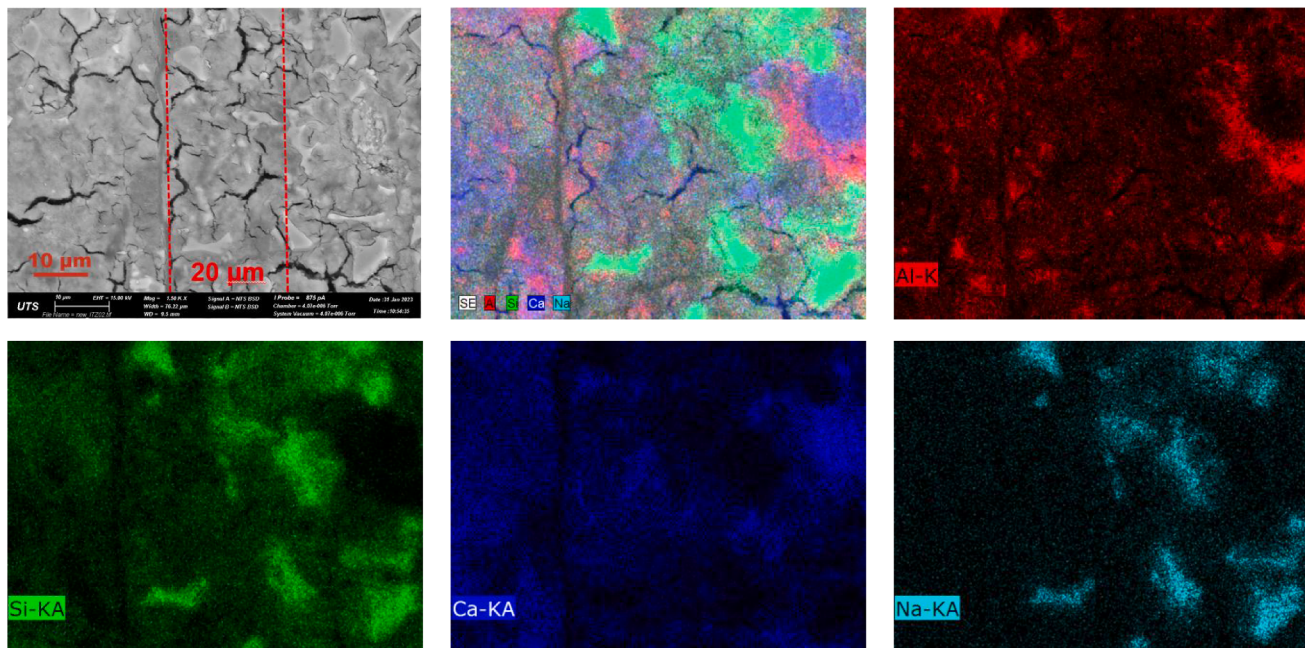
(a) Old ITZ

Fig. 9. EDS mapping analysis of ITZs.

(b) New ITZ without WGP

(c) New ITZ with WGP

Fig. 9. (*continued*).

ITZ and the matrix reduced. As a result, the number of effective points in the new ITZ and the matrix without WGP were both higher than old ITZ. In addition, the average Si/Ca ratio in the two regions reached around 1.0 in Fig. 10 (c) and (d). When 20% of the cement in the sample was replaced by WGP, the Si/Na ratio reduced, and the Si/Ca ratio increased significantly to around 1.5 as shown in Fig. 10 (e) and (f). Cement dilution as well as unreacted glass clinkers were important factors for the above element ratio changes [55]. However, it cannot be ignored that part of the WGP participated in the pozzolanic reaction, generating more C-S-H gel with high Si/Ca ratio, which enhanced the bonding strength of ITZ [56]. In addition, from the physical level, the rough and angular surface of the glass clinkers provided a natural place for the C-S-H nucleation reaction, which promotes the cement hydration, thereby increasing the overall Si/Ca ratio [57].

4.2.3. TG-DTG analysis

The new mortar part of the sample was cut out and ground into powder for TG tests in this section and ^{29}Si NMR tests in Section 3.2.4. Although the chemical composition in the new ITZs cannot be understood exactly, the influence of WGP on the performance of ITZs can still be deduced indirectly through the analysis of the new mortar matrix.

Fig. 11 shows the TG-DTG results for new mortar with and without

WGP. The apparent mass loss at 100–150 ℃, 385–440 ℃ and 600–690 ℃ represent the decomposition of C-S-H/AFt, Portlandite and Calcite, respectively [58]. From the results of DTG analysis, it can be clearly found that the content of CH in the new mortar containing WGP was lower than that of the new mortar without WGP. Moreover, the C-S-H/AFt content of new mortar containing WGP was slightly higher than that of the counterpart. These results were consistent with the EDS chemical elemental analysis in section 3.2.2. WGP consumed CH in the mortar and generated C-S-H/AFt, which helped to improve the cohesion and density of ITZs. In addition, WGP increased the mass ratio of $CaCO_3$ in the new mortar.

To further confirm the hydration degree of the two groups of mortar, the total amount of CH (including the existing portion and the portion transformed into $CaCO_3$) and nonevaporable water were calculated by Eqs. (4) and (5) [59,60]. The results were shown in Fig. 11 (b).

$$CH = \frac{74}{18} \bullet \frac{M_{440} - M_{385}}{M_0} + \frac{74}{44} \bullet \frac{M_{690} - M_{600}}{M_0} \qquad (4)$$

$$NEW = \frac{M_{1000} - M_{105}}{M_0} \qquad (5)$$

Among the equations, M_0 represents the initial mass of the sample;
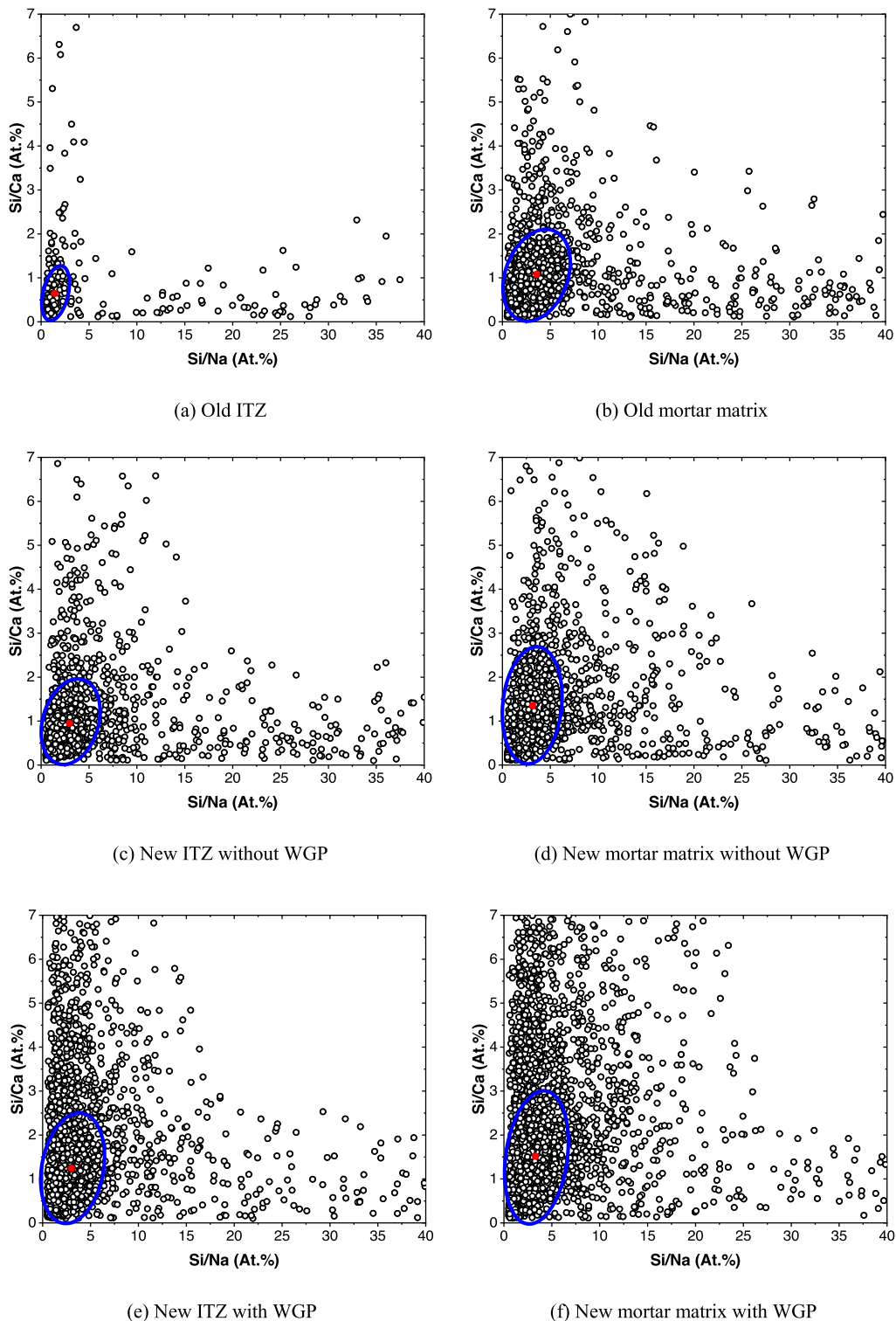
Fig. 10. Atomic proportions of element statistical results in ITZs and mortar matrix.
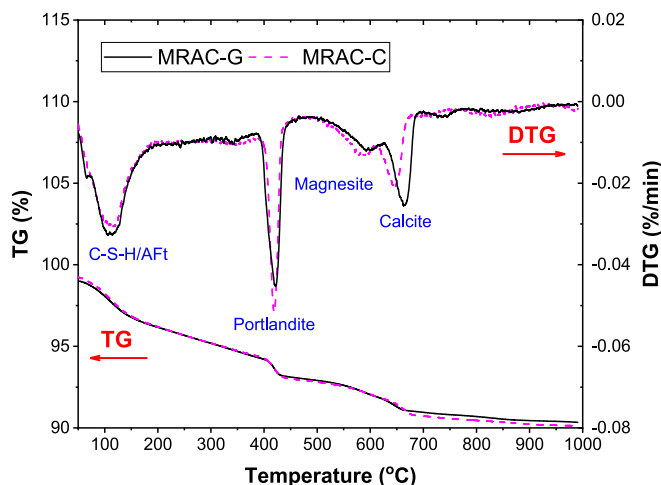
M_x represents the residual mass of the sample at × ℃; The numbers 74, 18 and 44 represent the relative molecular weight of CH, water, and CO_2 respectively.

According to Fig. 11 (b), the mass fractions of CH and nonevaporable water in the new mortar with WGP decreased 1.16% and 0.36%, respectively, compared with the new mortar without WGP. In cement paste containing SCM, nonevaporable water is contributed by cement hydration and replacement material [61]. It is reported that smaller
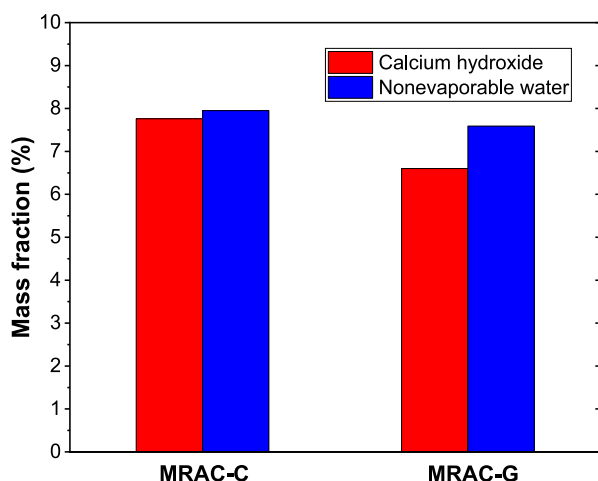
amounts of additional water were required in pozzolanic reaction than cement hydration [61]. The decrease of the proportion of nonevaporable in the mortar containing WGP combined with the variation of C-S-H and CH contents proved the existence of pozzolanic reaction.

4.2.4. ^{29}Si NMR characterisation analysis

The ^{29}Si NMR spectra and corresponding deconvolution results of samples with and without WGP are shown in Fig. 12 and Table 5. The

(a) TG-DTG curves
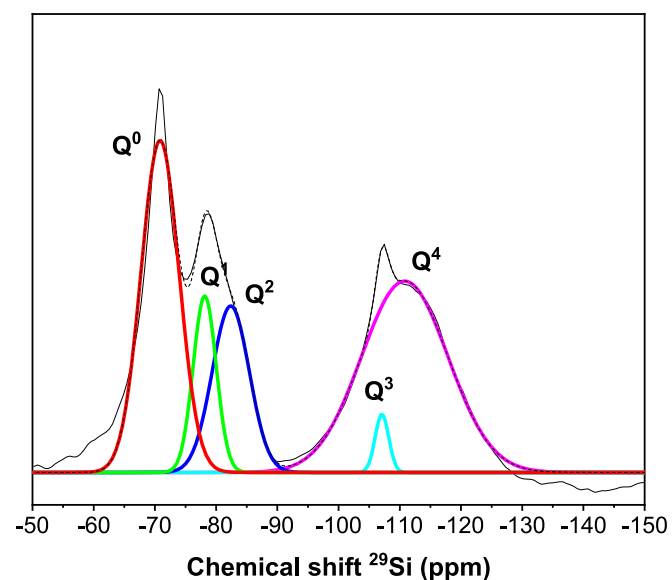
(b) Quantitative analysis of TG results

Fig. 11. TG and DTG results of new mortar with and without WGP.

(a) New mortar without WGP

(b) New mortar with WGP

Fig. 12. ^{29}Si NMR spectra of new mortar with and without WGP.

Table 5
Statistical deconvolution results of ^{29}Si NMR spectra.

	Q^0	Q^1	Q^2	DoH	PD	MCL
New mortar without WGP	55.2%	17.8%	27.0%	44.8%	1.38	5.03
New mortar with WGP	20.9%	27.1%	52.0%	79.1%	1.59	5.84
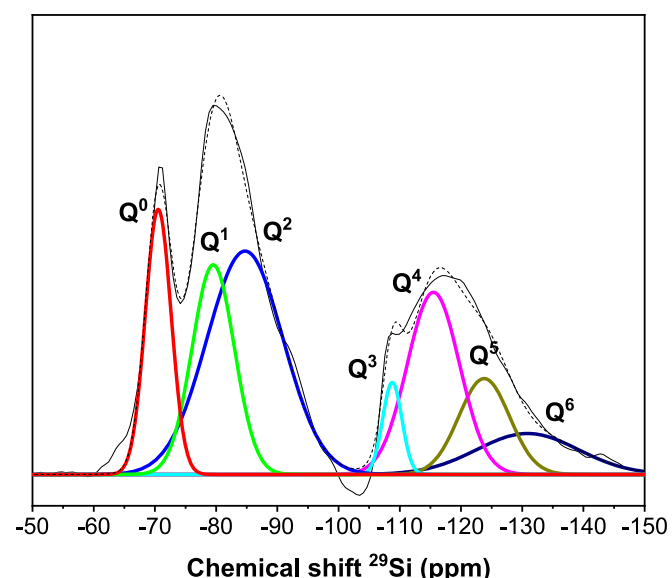
^{29}Si NMR reflected the bonding relations between Si and O in cementitious materials [62]. A silicon chain can be represented by Q^n, and the number 'n' corresponds to the number of $(SiO_4)^{4-}$ units attached to the central $(SiO_4)^{4-}$ tetrahedral units [62]. The complex degree of the silicate chain improved with the number of units, and the chemical shift became more negative [63]. Q^3-Q^6 corresponded to quartz and silicon-rich impurities. Here we only focus on the Si chains most directly related to Portland cement hydration, including Q^0, Q^1 and Q^2, whose chemical shifts were at around −70 ppm, −80 ppm and −85 ppm, respectively [64]. The Gaussian distribution area frictions of Q^3-Q^6 were deducted, and the remaining proportions were adjusted. Q^0 could be considered as the unreacted cement clinkers (C_2S and C_3S) [64,65]. Q^1 and Q^2 refer to the end-chain unit and middle-chain unit of C-S-H gel [64,65].

The peaks of soda-lime glass and unreacted cement clinkers overlapped [64]. In Fig. 12, the Q^0 peak of the sample containing WGP decreased, while the Q^1 and Q^2 peak improved compared with the sample powder without WGP, indicating that amorphous SiO_2 in WGP reacted with incompletely hydrated cement clinker to generate more C-S-H gel. In addition, WGP can also contribute to cement hydration to generate more C-S-H gel due to filler effect [57].

According to the relative intensities of Q^0, Q^1 and Q^2, the degree of hydration (DoH) of silicate phase, the polymerization degree (PD) of C-S-H and the mean chain length (MCL) of the silicate chain can be calculated [64]. The relative equations are as follows:
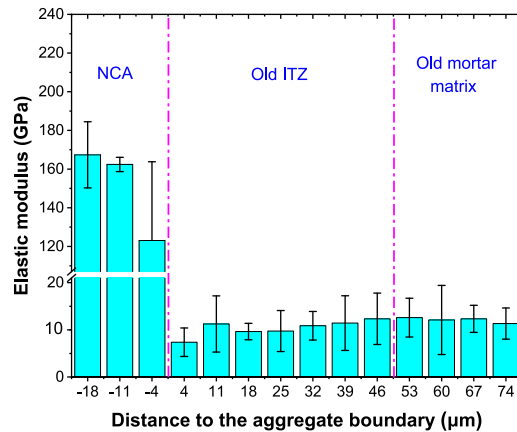
$$DoH = 100\% - Q^0 \tag{6}$$

$$PD = Q^1 + \frac{2 \times Q^2}{Q^1 + Q^2} \quad (7)$$
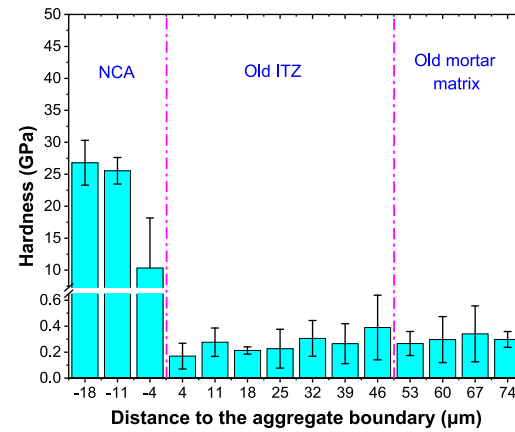
$$MCL = 2 \times \frac{Q^1 + Q^2}{Q^1} \quad (8)$$

The quantitative analysis results in Table 5 show that the hydration
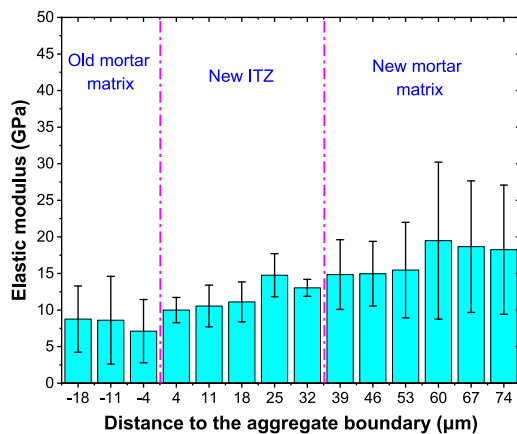
degree of silicate phase and polymerization degree of C-S-H in the sample with 20% WGP improved by 34.3% and 0.21, respectively, compared with the sample without WGP. In addition, the increase of the mean length of silicate chains in new mortar with WGP reflected the formation of denser and more stable C-S-H gel [64]. This explains why there were more hydration products and less pores/cracks in new ITZs
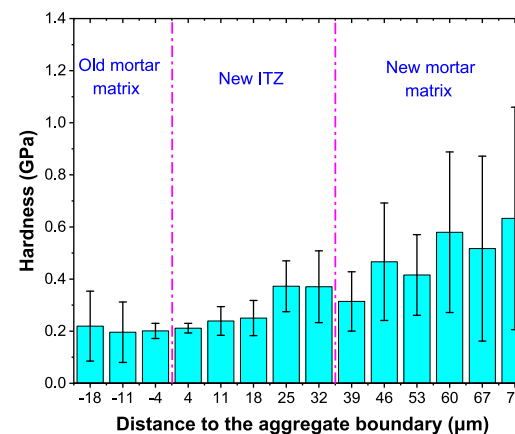
(a) Modulus of old ITZ
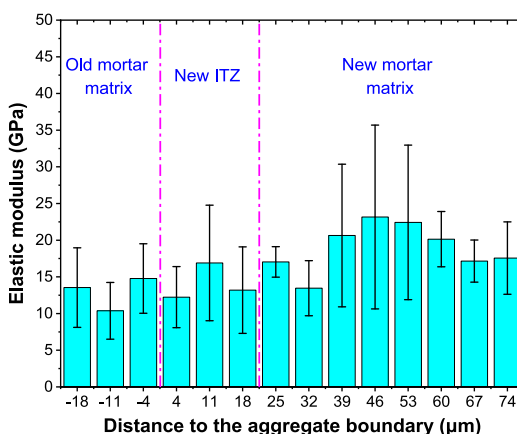
(b) Hardness of old ITZ
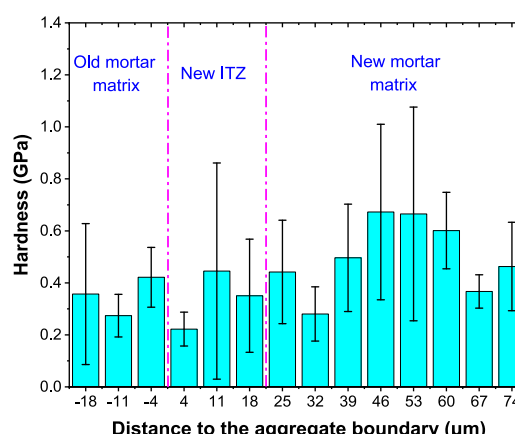
(c) Modulus of new ITZ without WGP

(d) Hardness of new ITZ without WGP

(e) Modulus of new ITZ with 20% WGP

(f) Hardness of new ITZ with 20% WGP

Fig. 13. Grid nanoindentation test results of modelled ITZs.

containing WGP in image analysis. To summarize, the TG-DTG and ^{29}Si NMR test results supported the deductions in Section 3.1 and Section 3.2.1 about the functions of WGP in new ITZs.

4.3. Micromechanical properties of ITZs

The nanoindentation test results with ITZ widths identified in Section 3.1 are shown in Fig. 13. The NCA adopted in this study was granite with the elastic modulus exceeding 160 GPa and the hardness over 25

GPa. It is worth noting that there was a clear drop in micromechanical properties on the edge of the modelled NCA, but not where the old mortar matrix adjacent to new ITZs. This could be explained that the elastic modulus and hardness of NCA chosen in this experiment were significantly higher than old mortar matrix. Old ITZ cannot provide enough restraint on the NCA edge. As a result, the value of the third column in Fig. 13 (a) and (b) NAC region was evidently lower than the first two columns. It can also be found that the average elastic modulus and hardness of old ITZ were slightly lower than old mortar matrix, and

(a) Old ITZ

(b) New ITZ without WGP

(c) New ITZ with WGP
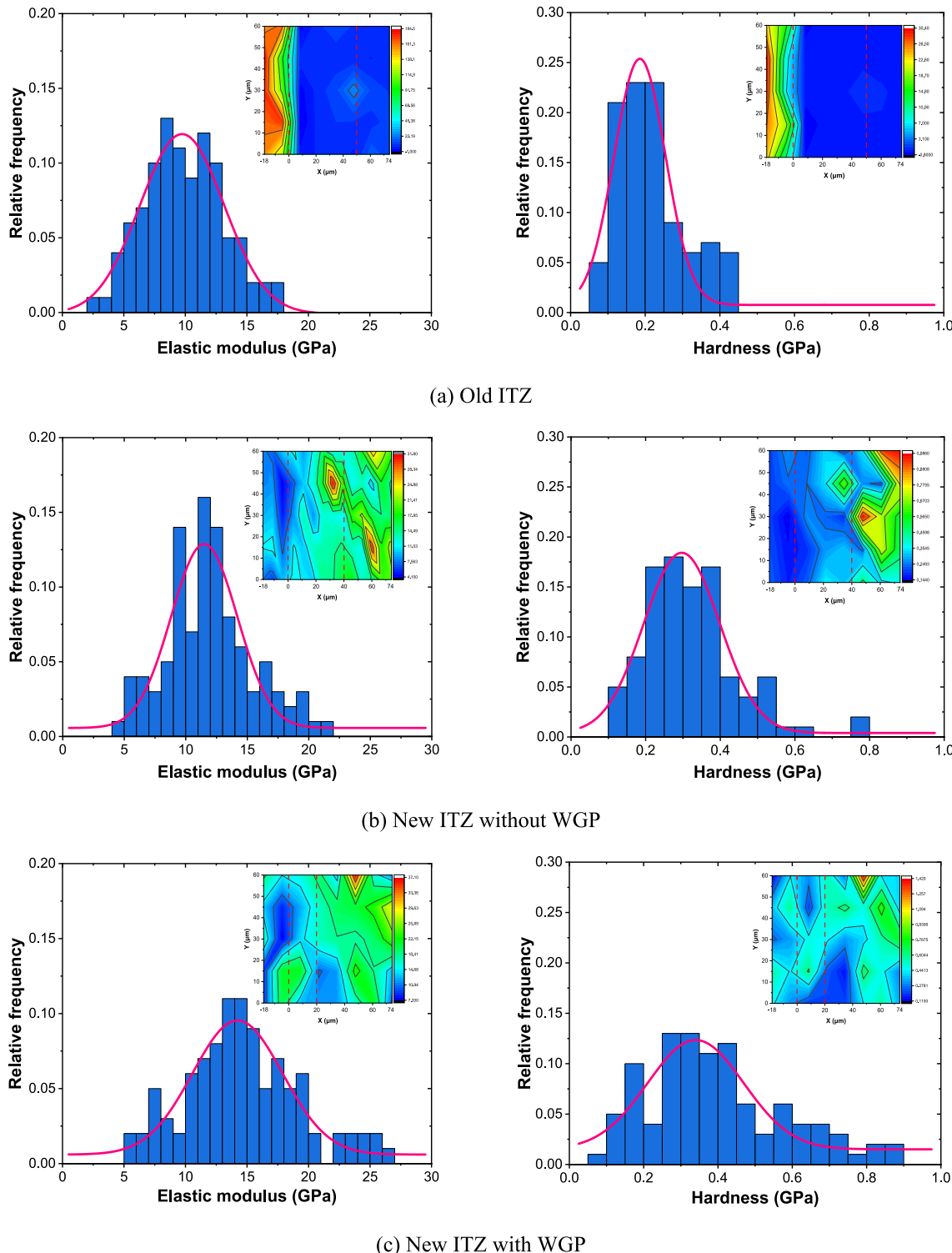
Fig. 14. Distribution of grid nanoindentation results in modelled ITZs.

the corresponding average elastic modulus and hardness ratios were 0.86 and 0.88, respectively. This is because of the 'wall effect' leading to a high water-cement ratio and low strength of old ITZ. Among them, the elastic modulus and hardness of old ITZ at 4 μm away from the surface of NCA were obviously lower than those far away from the surface of NCA. This corresponded to the local high water-cement ratio region near the NCA boundary observed in Fig. 9 (a).

As for MRAC without WGP, the average elastic modulus and hardness of new ITZ were 11.89 GPa and 0.29 GPa, respectively, which were slightly higher than those of the adjacent old mortar matrix (8.2 GPa and 0.2 GPa respectively). Although the 'wall effect' and release of pore water from the surface of RCA weakened the strength of the new ITZ, the lower initial water-cement ratio of the new ITZ still played a dominant role. Similar to the old ITZ, the micromechanical properties of the new ITZ were lower than those of the new mortar matrix (average elastic modulus ratio and hardness ratio were 0.69 and 0.71, respectively). In addition, the average elastic modulus and hardness of the new ITZ increased by 14.7% and 9.5%, respectively, compared with the old ITZ (10.37 GPa and 0.26 GPa), which confirmed the proposal to satisfy the strength requirements of RAC by reducing the water-cement ratio of the new mortar in real infrastructure construction.

As shown in Fig. 13 (e) and (f) the average elastic modulus of the new ITZ with WGP and the adjacent old mortar matrix was 14.11 GPa and 12.93 GPa, respectively. The average hardness was 0.34 and 0.35 GPa, respectively. As expected, WGP participated in the pozzolanic reaction, generating more C-S-H gels with a high Si/Ca ratio, which enhanced the strength and compactness of the new ITZ. It is worth noting that the micromechanical properties of the old mortar adjacent to the new ITZ with WGP were also enhanced compared to the old mortar adjacent to the new ITZ without WGP (average elastic modulus and hardness increased by 57.9% and 70.8% respectively). This can be partly attributed to the dissemination effect of amorphous silica in the new mortar with WGP. SiO$_2$ in the new mortar penetrated into the adjacent old mortar region and proceeded the pozzolanic reaction, so that the local old mortar performance was improved and achieved a tighter bond between old and new mortar. Furthermore, the 'wall effect' was also evident in the MRAC with WGP. The average elastic modulus and average hardness ratio of the new ITZ to the new mortar matrix were 0.74 and 0.68, respectively. In addition, the data fluctuation of columns in the new ITZ containing WGP was more significant than old ITZ and new ITZ without WGP. A small amount of unreacted WGP particles may still hid under the observation surface. According to Bosque et al. [24], the nanoindentation elastic modulus of glass was up to 86.17 GPa, which was significantly higher than that of cement products. The heterogeneity of cement paste containing WGP could pose a certain degree of influence on the results of nanoindentation test.

The nanoindentation test results were collected and presented in Fig. 14 in the form of frequency distribution histograms and contour maps. The elastic modulus and hardness of ITZ roughly follows the normal distribution. Therefore, the Gaussian model was used to fit the frequency histogram of the nanoindentation test results. The elastic modulus and hardness of the old ITZ were mainly distributed around 5–15 GPa and 0.2 GPa. The elastic modulus and hardness of the new ITZ without WGP increased slightly compared with the old ITZ. The values in the new ITZ with WGP were scattered in a larger range, and the overall elastic modulus and hardness were higher than those of the old ITZ and the new ITZ without WGP. In the contour maps of new ITZs with and without WGP, there were points with higher elastic modulus and hardness than surrounding area. This revealed the existence of CH and glass clinkers in the sample.

5. Discussions

Two groups of MRAC samples were fabricated and three ITZs were simulated in this study. In order to conduct a more comprehensive and detailed comparative analysis, the properties of the three ITZs were investigated from microscopic morphology, chemical and micromechanical properties. The sketch of three ITZs are shown in Fig. 15.

The test results of the old ITZ were basically consistent with the performance of the traditional ITZs [22,23,48]. The width of the old ITZ was around 50 μm. In addition, the old ITZ had a higher porosity than the old mortar matrix as shown in Fig. 15 (a). As a result, the cohesion of the old ITZ was the worst in the whole old mortar area. Meanwhile, due to extremely poor water absorption of granite, the free water in the mortar and attached on the surface of the natural aggregate was easy to accumulate on the boundary, forming a local cement paste region with a high water-cement ratio. These factors were shown in the nanoindentation tests as the lower average elastic modulus and hardness of the old ITZ than that of the mortar matrix. Moreover, the region closes to the natural aggregate surface along the old ITZ had the weakest mechanical properties. In some extreme cases [48,49], a debonding phenomenon occurred at the ITZs. On the one hand, it may be due to the non-uniform shrinkage between the natural aggregate and the mortar, leading to gaps along the aggregate boundary [30]. On the other hand, the soft character of cement paste near the aggregate boundary was likely to be removed during the grinding and polishing process, forming a gap where the cement paste seemed to be completely peeled off from the aggregate under an electron microscope [39]. However, in some studies, there was also the case that the ITZ microstructure was not different from the cement paste and the micromechanical properties of ITZ were even stronger than the mortar matrix [30,32]. The authors who came to these conclusions explained that the incompletely hydrated CH in the cement paste filled the pores within the ITZ and exhibited higher strength in nanoindentation tests [30,32]. In fact, CH has almost no cohesion properties and it would not affect the final result of the ITZ being the weakest zone in ordinary concrete [66,67]. In this study, the old mortar was cured for more than two months under the standard environment, and the cement paste achieved a higher hydration degree. Therefore, the difference in micromechanical properties between the old ITZ and the old mortar matrix was more obvious.

New mortar was prepared with a lower water-cement ratio than old mortar in this study. The effect of water-cement ratio on the mechanical properties and durability of RAC corresponds to the microscopic performance [22]. In Fig. 10, the number of effective points and Si/Ca ratio of C-S-H in the new ITZ without WGP was slightly higher than those in the old ITZ, indicating stronger C-S-H cohesion strength [54]. In the nanoindentation test, the new ITZ without WGP also exhibited higher elastic modulus and hardness than the old ITZ. The image analysis in Section 3.1 also shows that the width of the new ITZ was slightly lower than that of the old ITZ. These test results were all due to the low water-cement ratio reducing the distance between cement clinkers. However, in Fig. 8, the volume fraction of pores and cracks in the new ITZ was higher than that in the old ITZ. This seems to contradict the above conclusion of high cohesion strength of C-S-H in the new ITZ without WGP. For the new ITZ, in fact, due to the microstructure characteristics of the cement mortar, it was impossible to achieve the same degree of flatness on the old mortar as the modelled NCA surface by only grinding and polishing work [5]. There would inevitably be many pores and gaps on the surface of the old mortar. To fill the pores on the surface of the old mortar, the new ITZs were likely to form more pores and cracks, which reduced the effective bonding area between the old and new mortar in Fig. 15 (b). This is consistent with the theory that when fresh concrete fills moulds, many pores will be generated inside, and the air bubbles need to be removed by vibration. However, these pores may not be detected in nanoindentation tests. Because the regions with high porosity and large cracks were avoided in nanoindentation. In addition, when the indenter was stuck into a hole, the facility may not obtain a value or the load-indentation depth curve seriously deformed [23]. As a result, the nanomechanical properties of the new ITZ still remained at a high level, although possessed a high porosity.

For the new ITZ with WGP, all the results show a significant improvement in micro performance compared to the old ITZ and the

(a) Old ITZ   (b) New ITZ without WGP   (c) New ITZ with WGP
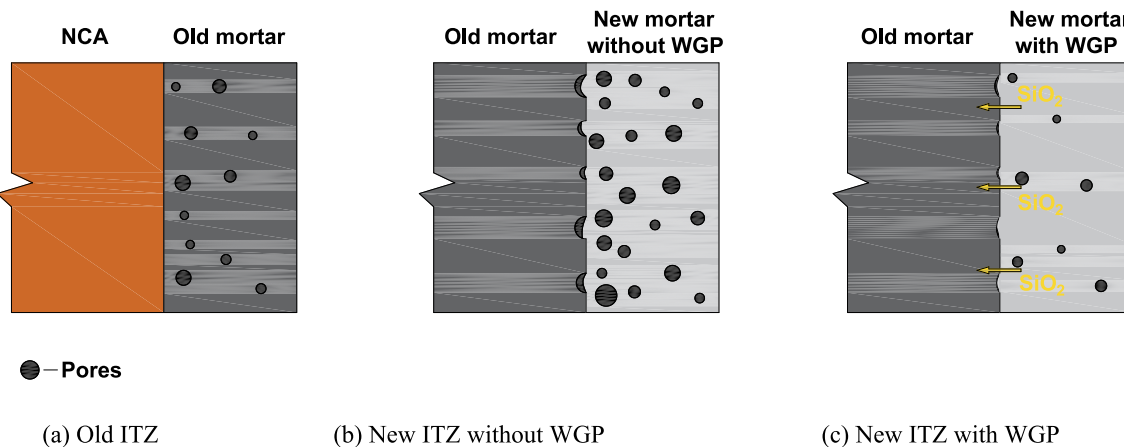
Fig. 15. ITZs microstructure general view and WGP enhancement mechanism.

new ITZ without WGP. Searching the previous research results and combining the conclusions obtained from the TG and NMR test results in this study, it can be easily concluded that WGP accelerated cement hydration from both physical and chemical level to generate more high Si/Ca ratio C-S-H gel, which provided enough bonding strength between old and new mortar [3]. In addition, according to Fig. 8, it can be found that different from the new ITZ without WGP, the porosity of the new ITZ after adding WGP was lower than that of the old ITZ. In addition to the pozzolanic reaction induced by WGP to make the new ITZ more compact, free silica in the new ITZ with WGP released into the adjacent old mortar, participated in the secondary hydration, and refined the flatness of the old mortar surface, as shown in Fig. 15 (c). Therefore, the negative influence of the surface porosity of the old mortar on the microstructure of the new ITZ was alleviated. Meanwhile, it has to be admitted that the pozzolanic activity of WGP was poor, and it need a long time to finish pozzolanic reaction according to some studies [3]. This is somewhat reflected in the nanoindentation test results in Fig. 13 (e) and (f). The influence of incompletely reacted glass particles on the porosity and micromechanical properties of new ITZ cannot be ignored.

In general, for the traditional ITZ, that is, the old ITZ in this study, the bonding strength of cement mortar to natural aggregate can be evaluated only based on the compactness or micromechanical properties of ITZs. Because the strong cohesiveness of C-S-H gel corresponds to the high compactness. However, for the new ITZs in RAC, there could be conditions with high C-S-H cohesion strength but high porosity at the same time. It is unreliable to only rely on a single indicator to evaluate the bonding strength between old and new mortar. Besides, the weak bonding of C-S-H gel to unreacted clinkers should also be considered. In future research, it is necessary to comprehensively evaluate the bonding performance between old and new mortar through effective contact area and cohesion strength of C-S-H gel.

6. Conclusions

In this study, MRAC samples were fabricated to simulate regular ITZs. In order to distinguish the interface between the old and new mortar easily, the new mortar adopted a lower water-cement ratio. The performance of old and new ITZs was compared by using statistical techniques and multiscale experimental methods. Meanwhile, the improvement efficiency of WGP on the new ITZ properties was evaluated. The related conclusions can be drawn up as below:

(1) The regular natural aggregate-old mortar and old mortar-new mortar interfaces produced in this study can be clearly observed under an electron microscope. Modelled ITZ effectively reduced unnecessary workload as well as achieved satisfactory accuracy of test results. The sample preparation procedure in this study is sufficient to meet the testing requirements for BSE and nanoindentation tests.

(2) Morphological analysis revealed that the widths of the old ITZ, the new ITZ without WGP and the new ITZ with WGP were around 50, 40, and 20 μm, respectively. The volume fraction of cracks and pores in the new ITZ without WGP was 7.29%, which was higher than 4.33% in the old ITZ, while the content of the reaction was similar, around 80.5%. In comparison, the proportion of pores and unreacted products within the new ITZ with WGP decreased to 4.30% and 10.27%, and the content of reaction products increased to 85.43%.

(3) In the ANOVA of the phase distribution, the volume fractions difference of reaction and unreacted products were extremely significant for the old and new ITZ without WGP compared with the corresponding mortar matrix (P values lower than 0.01), while for the new ITZ with WGP, only the porosity was significantly different from that in the new mortar matrix (P value was between 0.01 and 0.05). In the comparison between different ITZs, WGP can increase the difference significance in the reaction products.

(4) The chemical and mineralogical analysis showed that the hydration of cement clinkers in the three types of ITZs reached a high level. The Si/Ca ratio in the new ITZ without WGP was around 1.0, which was slightly higher than that of the old ITZ (0.6 on average). WGP can effectively promote hydration and pozzolanic reaction from physical and chemical level to generate a large amount of C-S-H with a Si/Ca ratio of around 1.5, which provided stronger cohesion strength for the ITZ.

(5) Nanoindentation tests well reflected the influence of the 'wall effect' on the micromechanical properties of ITZ. The average elastic modulus and hardness of the three ITZs were lower than those of the corresponding mortar matrix. The elastic modulus and hardness of the new ITZ without WGP were 11.89 GPa and 0.29 GPa, which were higher than old ITZ (10.37 GPa and 0.26 GPa) due to the lower water-cement ratio used in new mortar. Besides, WGP can largely improve the elastic modulus and hardness of new ITZs to 14.11 GPa and 0.34 GPa respectively.

(6) There were more exposed pores on the surface of the old mortar, which led to the fact that the bond between the old and new mortar cannot be as tight as that between old mortar and natural aggregate. Moreover, many pores were formed in the new ITZ without WGP. After adding 20% WGP to the new mortar, amorphous silica improved the performance of the new ITZ as well as penetrated into the adjacent old mortar to accelerate the pozzolanic reaction. The surface structure of the old mortar was thus also improved. To evaluate the bonding strength between old and

new mortar in RAC, not only the cohesion of C-S-H gel, but also the effective contact area should be considered.

CRediT authorship contribution statement

Hanbing Zhao: Conceptualization, Formal analysis, Investigation, Writing – original draft, Writing – review & editing. **Wengui Li:** Conceptualization, Funding acquisition, Resources, Supervision, Validation, Writing – original draft, Writing – review & editing. **Yixiang Gan:** Resources, Validation, Writing – original draft, Writing – review & editing. **Kejin Wang:** Supervision, Validation, Writing – original draft, Writing – review & editing. **Zhiyu Luo:** Methodology, Validation, Writing – original draft, Writing – review & editing.

Declaration of Competing Interest

The authors declare that they have no known competing financial interests or personal relationships that could have appeared to influence the work reported in this paper.

Data availability

Data will be made available on request.

Acknowledgements

References

[1] Z. Tang, W. Li, V.W.Y. Tam, C. Xue, Advanced progress in recycling municipal and construction solid wastes for manufacturing sustainable construction materials, Resour. Conserv. Recycl. 6 (2020), 100036.

[2] B. Wang, L. Yan, Q. Fu, B. Kasal, A Comprehensive Review on Recycled Aggregate and Recycled Aggregate Concrete, Resour. Conserv. Recycl. 171 (2021), 105565.

[3] W. Dong, W. Li, Z. Tao, A comprehensive review on performance of cementitious and geopolymeric concretes with recycled waste glass as powder, sand or cullet, Resour. Conserv. Recycl. 172 (2021), 105664.

[4] V. Corinaldesi, G. Moriconi, Influence of mineral additions on the performance of 100% recycled aggregate concrete, Constr. Build. Mater. 23 (8) (2009) 2869–2876.

[5] Z. Tang, Y. Hu, V.W.Y. Tam, W. Li, Uniaxial compressive behaviors of fly ash/slag-based geopolymeric concrete with recycled aggregates, Cem. Concr. Compos. 104 (2019), 103375.

[6] Z. Tang, W. Li, V.W.Y. Tam, L. Yan, Mechanical performance of CFRP-confined sustainable geopolymeric recycled concrete under axial compression, Eng. Struct. 224 (2020), 111246.

[7] L. Li, J. Lu, P. Shen, K. Sun, L.E.L. Pua, J. Xiao, C.S. Poon, Roles of recycled fine aggregate and carbonated recycled fine aggregate in alkali-activated slag and glass powder mortar, Constr. Build. Mater. 364 (2023), 129876.

[8] Y. Hu, Z. Tang, W. Li, Y. Li, V.W.Y. Tam, Physical-mechanical properties of fly ash/GGBFS geopolymer composites with recycled aggregates, Constr. Build. Mater. 226 (2019) 139–151.

[9] F.G. Cabrera-Covarrubias, J.M. Gómez-Soberón, C.A. Rosas-Casarez, J.L. Almaral-Sánchez, J.M. Bernal-Camacho, Recycled Mortars with Ceramic Aggregates. Pore Network Transmutation and Its Relationship with Physical and Mechanical Properties, Materials 14 (1543) (2021) 14061543.

[10] G.L. Golewski, B. Szostak, Strength and microstructure of composites with cement matrixes modified by fly ash and active seeds of C-S-H phase, Struct. Eng. Mech. 82 (4) (2022) 543–556.

[11] G.L. Golewski, Combined Effect of Coal Fly Ash (CFA) and Nanosilica (nS) on the Strength Parameters and Microstructural Properties of Eco-Friendly Concrete, Energies 16 (452) (2023) 16010452.

[12] G.L. Golewski, Fracture Performance of Cementitious Composites Based on Quaternary Blended Cements, Materials 15 (6023) (2022) 15176023.

[13] A. Omran, A., Tagnit-Hamou Performance of glass-powder concrete in field applications, Constr. Build. Mater. 109 (2016) 84–95.

[14] Z.Z. Ismail, E.A., AL-Hashmi,, Recycling of waste glass as a partial replacement for fine aggregate in concrete, Waste Manage. 29 (2009) 655–659.

[15] M.J. Chinchillas-Chinchillas, C.A. Rosas-Casarez, S.P. Arredondo-Rea, J.M. Gómez-Soberón, R., Corral-Higuera SEM Image Analysis in Permeable Recycled Concretes with Silica Fume. A Quantitative Comparison of Porosity and the ITZ, Materials 12 (2201) (2019) 12132201.

[16] P. Vargas, O. Restrepo-Baena, J.I. Tobón, Microstructural analysis of interfacial transition zone (ITZ) and its impact on the compressive strength of lightweight concretes, Constr. Build. Mater. 137 (2017) 381–389.

[17] M. Wang, Y. Xie, G. Long, C. Ma, X. Zeng, Microhardness characteristics of high-strength cement paste and interfacial transition zone at different curing regimes, Constr. Build. Mater. 221 (2019) 151–162.

[18] G. Fang, M. Zhang, The evolution of interfacial transition zone in alkali-activated fly ash-slag concrete, Cem. Concr. Res. 129 (2020), 105963.

[19] Z. Tang, W. Li, V.W.Y. Tam, Z. Luo, Investigation on dynamic mechanical properties of fly ash/slag-based geopolymeric recycled aggregate concrete, Compos. B Eng. 185 (2020), 107776.

[20] S.R. da Silva, J. de Brito, J.J. de Oliveira Andrade, Synergic effect of recycled aggregate, fly ash, and hydrated lime in concrete production, J. Build. Eng. 70 (2023), 106370.

[21] Z. Luo, W. Li, K. Wang, S.P. Shah, Research progress in advanced nanomechanical characterization of cementbased materials, Cem. Concr. Compos. 94 (2018) 277–295.

[22] J. Xiao, W. Li, Z. Sun, D.A. Lange, S.P. Shah, Properties of interfacial transition zones in recycled aggregate concrete tested by nanoindentation, Cem. Concr. Compos. 37 (2013) 276–292.

[23] W. Li, J. Xiao, Z. Sun, S. Kawashima, S.P. Shah, Interfacial transition zones in recycled aggregate concrete with different mixing approaches, Constr. Build. Mater. 35 (2012) 1045–1055.

[24] I.F. Saez del Bosque, W. Zhu, T. Howind, A. Matías, M.I. Sanchez de Rojas, C. Medina, Properties of interfacial transition zones (ITZs) in concrete containing recycled mixed aggregate, Cem. Concr. Compos. 81 (2017) 25–34.

[25] Z. Pan, Z. Tao, T. Murphy, R. Wuhrer, High temperature performance of mortars containing fine glass powders, J. Clean. Prod. 162 (2017) 16–26.

[26] G.L. Golewski, An extensive investigations on fracture parameters of concretes based on quaternary binders (QBC) by means of the DIC technique, Constr. Build. Mater. 351 (2022), 128823.

[27] Y. Kong, P. Wang, S. Liu, G. Zhao, Y. Peng, SEM Analysis of the Interfacial Transition Zone between Cement-Glass Powder Paste and Aggregate of Mortar under Microwave Curing, Materials 9 (9) (2016) 733–745.

[28] H. Du, K.H. Tan, Properties of high volume glass powder concrete, Cem. Concr. Compos. 75 (2017) 22–29.

[29] D. Mostofinejad, S.M. Hosseini, F. Nosouhian, T. Ozbakkaloglu, B.N. Tehrani, Durability of concrete containing recycled concrete coarse and fine aggregates and milled waste glass in magnesium sulfate environment, J. Build. Eng. 29 (2020), 101182.

[30] Z. Luo, W. Li, K. Wang, A. Castel, S.P. Shah, Comparison on the properties of ITZs in fly ash-based geopolymer and Portland cement concretes with equivalent flowability, Cem. Concr. Res. 143 (2021), 106392.

[31] Z. Luo, W. Li, K. Wang, A. Castel, S.P. Shah, Nano/micromechanical characterisation and image analysis on the properties and heterogeneity of ITZs in geopolymer concrete, Cem. Concr. Res. 152 (2022), 106677.

[32] S. Diamond, J. Huang, The ITZ in concrete-a different view based on image analysis and SEM observations, Cem. Concr. Compos. 23 (2-3) (2001) 179–188.

[33] S.P. Shah, G. Winter, Inelastic behavior and fracture of concrete, ACI Mater. J. 63 (9) (1966) 925–930.

[34] J. Xiao, W. Li, D.J. Corr, S.P. Shah, Effects of interfacial transition zones on the stress–strain behavior of modeled recycled aggregate concrete, Cem. Concr. Res. 52 (2013) 82–99.

[35] C. Fu, Y. Ling, K., Wang An innovation study on chloride and oxygen diffusions in simulated interfacial transition zone of cementitious material, Cem. Concr. Compos. 110 (2020), 103585.

[36] B. Zhan, B. Xuan, C.S. Poon, K.L. Scrivener, Characterization of interfacial transition zone in concrete prepared with carbonated modeled recycled concrete aggregates, Cem. Concr. Res. 136 (2020), 106175.

[37] W. Li, Z. Luo, Y. Gan, K. Wang, S.P. Shah, Nanoscratch on mechanical properties of interfacial transition zones (ITZs) in fly ash-based geopolymer composites, Compos. Sci. Technol. 214 (2021), 109001.

[38] B. Lei, W. Li, Z. Tang, V.W.Y. Tam, Z. Sun, Durability of recycled aggregate concrete under coupling mechanical loading and freeze-thaw cycle in salt-solution, Constr. Build. Mater. 163 (2018) 840–849.

[39] K. Lyu, E.J. Garboczi, W. She, C. Miao, The effect of rough vs. smooth aggregate surfaces on the characteristics of the interfacial transition zone, Cem. Concr. Compos. 99 (2019) 49–61.

[40] W.C. Oliver, G.M. Pharr, Improved technique for determining hardness and elastic modulus using load and displacement sensing indentation experiments, J. Mater Res. 7 (6) (1992) 1564–1583.

[41] Y. Kim, A. Hanif, M. Usman, W., Park Influence of bonded mortar of recycled concrete aggregates on interfacial characteristics – Porosity assessment based on pore segmentation from backscattered electron image analysis, Constr. Build. Mater. 212 (2019) 149–163.

[42] K. Lyu, W. She, C. Miao, H. Chang, Y. Gu, Quantitative characterization of pore morphology in hardened cement paste via SEM-BSE image analysis, Constr. Build. Mater. 202 (2019) 589–602.

[43] K.L. Scrivener, Backscattered electron imaging of cementitious microstructures: understanding and quantification, Cem. Concr. Compos. 26 (8) (2004) 935–945.

[44] H.S. Wong, M.K. Head, N.R. Buenfeld, Pore segmentation of cement-based materials from backscattered electron images, Cem. Concr. Res. 36 (6) (2006) 1083–1090.

[45] H.S. Wong, N.R. Buenfeld, Euclidean Distance Mapping for computing microstructural gradients at interfaces in composite materials, Cem. Concr. Res. 36 (6) (2006) 1091–1097.

[46] H.S. Wong, N.R. Buenfeld, Determining the water–cement ratio, cement content, water content and degree of hydration of hardened cement paste: Method development and validation on paste samples, Cem. Concr. Res. 39 (10) (2009) 957–965.

[47] J. Thomas, N.N. Thaickavil, P.M. Wilson, Strength and durability of concrete containing recycled concrete aggregates, J. Build. Eng. 19 (2018) 349–365.

[48] M. Khedmati, Y. Kim, J.A. Turner, Investigation of the interphase between recycled aggregates and cementitious binding materials using integrated microstructuralnanomechanical-chemical characterization, Compos. B Eng. 158 (2019) 218–229.

[49] M. Khedmati, Y.R. Kim, J.A. Turner, H. Alanazia, C. Nguyen, An integrated microstructural-nanomechanical-chemical approach to examine material-specific characteristics of cementitious interphase regions, Mater. Charact. 138 (2018) 154–164.

[50] C. Camposeco-Negrete, Optimization of cutting parameters for minimizing energy consumption in turning of AISI 6061 T6 using Taguchi methodology and ANOVA, J. Clean. Prod. 53 (2013) 195–203.

[51] K. Giasin, S., Ayvar-Soberanis An Investigation of burrs, chip formation, hole size, circularity and delamination during drilling operation of GLARE using ANOVA, Compos. Struct. 159 (2017) 745–760.

[52] P.R. Rangaraju, J. Olek, S. Diamond, An investigation into the influence of inter-aggregate spacing and the extent of the ITZ on properties of Portland cement concretes, Cem. Concr. Res. 40 (11) (2010) 1601–1608.

[53] C.H. Chen, R. Huang, J.K. Wu, C.C. Yang, Waste E-glass particles used in cementitious mixtures, Cem. Concr. Res. 36 (3) (2006) 449–456.

[54] W. Kunther, S. Ferreiro, J. Skibsted, Influence of the Ca/Si ratio on the compressive strength of cementitious calcium–silicate–hydrate binders, J. Mater. Chem. A 5 (2017) 17401.

[55] M. Mejdi, W. Wilson, M. Saillio, T. Chaussadent, L. Divet, A. Tagnit-Hamou, Hydration and microstructure of glass powder cement pastes – A multi-technique investigation, Cem. Concr. Res. 151 (2022), 106610.

[56] Y. Jiang, T.C. Ling, K.H. Mo, C. Shi, A critical review of waste glass powder – Multiple roles of utilization in cement-based materials and construction products, J. Environ. Manag. 242 (2019) 440–449.

[57] M. Mirzahosseini, K.A. Riding, Influence of different particle sizes on reactivity of finely ground glass as supplementary cementitious material (SCM), Cem. Concr. Compos. 56 (2015) 95–105.

[58] F. Qu, W. Li, K. Wang, S. Zhang, D., Sheng Performance deterioration of fly ash/slag-based geopolymer composites subjected to coupled cyclic preloading and sulfuric acid attack, J. Clean. Prod. 321 (2021), 128942.

[59] L. Guo, J. Wu, H., Wang Mechanical and perceptual characterization of ultra-high-performance cement-based composites with silane-treated graphene nano-platelets, Constr. Build. Mater. 240 (2020), 117926.

[60] W. Dong, W. Li, Y. Guo, K. Wang, D. Sheng, Mechanical properties and piezoresistive performances of intrinsic graphene nanoplate/cement-based sensors subjected to impact load, Constr. Build. Mater. 327 (2022), 126978.

[61] J.I. Escalante-Garcia, Nonevaporable water from neat OPC and replacement materials in composite cements hydrated at different temperatures, Cem. Concr. Res. 33 (11) (2003) 1883–1888.

[62] D.C. MacLaren, M.A. White, Cement: Its Chemistry and Properties,, J. Chem. Educ. 80 (6) (2003).

[63] B. Lu, S. Drissi, J. Liu, X. Hu, B. Song, C. Shi, Effect of temperature on CO2 curing, compressive strength and microstructure of cement paste, Cem. Concr. Res. 157 (2022), 106827.

[64] L. Chen, Y. Zhang, L. Wang, S. Ruan, J. Chen, H. Li, J. Yang, V. Mechtcherine, D.C. W. Tsang, Biochar-augmented carbon-negative concrete, Chem. Eng. J. 431 (2022), 133946.

[65] A.F. Jamsheer, K. Kupwade-Patil, O. Büyüköztürk, A. Bumajdad, Analysis of engineered cement paste using silica nanoparticles and metakaolin using 29Si NMR, water adsorption and synchrotron X-ray Diffraction, Constr. Build. Mater. 180 (2018) 698–709.

[66] Z. Luo, W. Li, Y. Gan, K. Mendu, S.P. Shah, Maximum likelihood estimation for nanoindentation on sodium aluminosilicate hydrate gel of geopolymer under different silica modulus and curing conditions, Compos. B Eng. 198 (2020), 108185.

[67] Z. Luo, W. Li, Y. Gan, K. Mendu, S.P. Shah, Applying grid nanoindentation and maximum likelihood estimation for N-AS-H gel in geopolymer paste: Investigation and discussion, Cem. Concr. Res. 135 (2020), 106112.

[68] B. Wu, X. Yang, J.J. Zhang, G.M. Chen, X.Y. Zhao, Recycled lump concrete-filled FRP tubular columns: Axial compressive behavior and size effects, Constr. Build. Mater. 352 (2022) 129000.

[69] B. Wu, C.W. Peng, X.Y. Zhao, Cyclic loading tests of semi-precast circular steel tubular columns incorporating precast segments containing demolished concrete lumps, Eng. Struct. 211 (2020) 110438.

[70] B. Wu, S.M. Jian, X.Y. Zhao, Structural behavior of steel-concrete partially encased composite columns containing demolished concrete lumps under axial compression, Eng. Struct. 197 (2019) 109383.